A non-porous Fe(II) complex for the colorimetric detection of hazardous gases and the monitoring of meat freshness

Li Sun[a], Aurelian Rotaru[b], Yann Garcia*[,a]

[a] Institute of Condensed Matter and Nanosciences, Molecular Chemistry, Materials and Catalysis (IMCN/MOST), Université catholique de Louvain, 1348 Louvain-la-Neuve, Belgium.

[b] Department of Electrical Engineering and Computer Science and MANSiD Research Center, "Stefan cel Mare" University, University Street, 13, Suceava 720229, Romania

Email: yann.garcia@uclouvain.be

Abstract

Food quality monitoring and freshness assessment are critical for ensuring food safety at a large scale. Ammonia is used as an important indicator of protein rich food spoilage state. However, current ammonia gas sensors suffer from insufficient sensitivity and selectivity, or sophisticated instrumentation, hindering their practical application in in-situ and real-time food quality monitoring. To overcome such limitations, an innovative nonporous colorimetric complex **1** has been synthesized and investigated for the detection of $NH_{3(g)}$ and its volatile organic derivatives including aliphatic amines, 1,2-diaminopropane$_{(g)}$, isobutylamine$_{(g)}$ and ethylenediamine$_{(g)}$, etc. The sensor operates colorimetrically at room temperature without energy input, with a detection limit to ammonia$_{(g)}$ of 105 ppb, and show excellent reusability. The colorimetric detection mechanism involves a partial spin state change of Fe(II) ions upon exposure to amines in the gas phase. In addition, the complex was utilized as real-time monitoring of meat freshness using a smartphone. Thus, chemosensor **1** is considered as a ground breaking new-generation portable electronic nose for vapors of volatile organic compounds discrimination at room temperature.

Keywords: Colorimetric complexes, Cold channel control, Ammonia gas sensor, Sensitivity and selectivity, Meat freshness assessment.

1.Introduction

In recent years, with the continuous improvement of the quality of life, the demand for safety food and a healthier environment has been increasing, thus making food quality monitoring and assessment, as well as air quality issues, a constant concern.[1-3] It is well known that the spoilage process of high-protein foods (meat of pork, beef, chicken and fish, etc.) releases some volatile nitrogenous compounds (ammonia, trimethylamine, methylamine, cadaverine, putrescine, etc.), which is often accompanied by unpleasant odors.[4] These are mainly produced through the decarboxylation of various amino acids by the action of enzymes and microbial activities.[5-7] Degradation of proteins and other nitrogenous compounds as a result of spoilage of meat causes the accumulation of organic amines that are commonly known as total volatile basic nitrogen (TVB-N).[8] Among such molecules, ammonia is considered as a potential indicator of spoilage of protein-rich foods.[9] Although ammonia has a wide range of applications in industrial production,[10] it is also one of the most hazardous components of environmental pollutants, posing a wide range of threats to the ecological environment and human health.[11-15] It is therefore currently highly desirable to develop efficient, quantifiable, real-time, simple to operate, in-situ and low-cost ammonia gas detection methods.

Currently, numerous conventional analytical techniques have been used for meat safety analysis, including Raman spectroscopy,[16] Fourier transform infrared (FTIR) spectroscopy,[17] fluorescence spectroscopy,[18] high performance liquid chromatography,[19] gas chromatography-mass spectrometry,[20] etc. These detection techniques have great selectivity and sensitivity for analytes released during food spoilage, but actually suffer from a high purchase cost and sophisticated and laborious experimental setups, thus limiting their practical use outside the laboratory.[21] Other approaches for effective sensing of organic amines and meat freshness is given by sensors that use functionalized metal oxides,[6] conducting polymers, nanostructured[22] or metal-organic materials[23] to respond analytes from meat spoilage. For such sensing technology, the response of the sensor mainly depends on

the physical adsorption of analyte molecules on, or inside the sensor element, which causes changes in fluorescence intensity (optical sensors) or conductivity (electronic sensors and electronic nose).[24] The sensitivity of such fluorescent sensors is however limited given that the fluorescence quantum yields are relatively low.[22] Electronic sensors are also limited given that their sensitivity depends to changes in relative humidity, leading to output drift or complete failure.[25] Metal oxide nanostructures have been found to offer many advantages for ammonia gas sensing such as a high sensitivity, reliability and low costs. However, their high working temperature (150–500°C) and poor selectivity still restrict their wide application.[26-28] Alternatively, colorimetric gas sensors were proposed for the determination of ammonia for food spoilage[29,30] Such optical technology has been used for the rapid detection of hazardous gases given that it offer in-field and real-time options, do not require expensive equipment or cumbersome processes, and can detect target analytes at room temperature through color changes.

Recently, some Fe(II) coordination complexes have attracted increasing interest due to their unique chemical and physical properties, such as high catalytic activity, good selectivity, sensitivity and low cost under specific conditions to produce corresponding analytical signals. Thus, these have been used in various fields including catalysis,[31] batteries,[32] magnetic resonance imaging,[33] pollutants remediation, [34] etc. In recent years, it has been realized that some Fe(II) complexes could change their color after adsorbing different gases, i.e. which could be used as gas colorimetric sensors in the long term.[35] For instance, Burzurí *et al*.[36] developed a nonporous coordination polymer, $[Fe(H_2O)_2(CH_3CN)_2(pyrazine)](BF_4)_2 \cdot 2CH_3CN$, showing distinct optical response to different molecules (CH_3CN, H_2O and pyrrole), accompanied by a color change of the crystal from light yellow to orange. Garcia *et al.* also reported an Fe(II) system, $[Fe(trz\text{-}tet)_2(H_2O)_4] \cdot nH_2O$ (trz-tetH = 5-(4H-1,2,4-triazol-yl)-2H-tetrazole), which could distinguish among different toxic industrial chemicals (TICs).[37-39] Although these colorimetric sensors show significant color change after adsorption of different vapors, no real quantification of detected gas

molecules was made. It is therefore important to search for colorimetric sensors, not only for the detection and discrimination among a wide range of analytes showing an olfactory-like response but also with high sensitivity, which could be useful for meat spoilage detection.

Herein, we propose a simple strategy to fabricate a Fe(II) based colorimetric platform ($[Fe(Hbta)_2(H_2O)_2]\cdot 2H_2O$ (**1**) with **H_2bta** = bis(1H-tetrazol-5-yl)amine)[40]. It undergoes a color change when treated with some harmful vapor molecules (listed in Scheme S1), especially, ammonia and some amines vapors. This complex was used for NH_3 quantitative detection, in the frame of the visual real-time and in-situ monitoring of meat spoilage by a simple color recognizing smartphone software. Our findings open up new prospects for exploring various Fe(II) based materials for sensing hazardous and noxious substances, and shows tremendous promise in applications for food status monitoring and environmental quality assessment.

2. Experimental

2.1 Synthesis of nonporous $[Fe(Hbta)_2(H_2O)_2]\cdot 2H_2O$ (1)

Pale-blue block single crystals of **1** were obtained from the reaction of **H_2bta** and $FeCl_2\cdot 4H_2O$ in 5% HCl aqueous solution at room temperature after one day.[40] Yield: 82 mg (0.19 mmol. 76%). Elemental analysis for $C_4H_{12}FeN_{18}O_4$ (432.17 g/mol) (%): Calcd. C, 11.12; H, 2.80; N, 58.32; Found: C, 11.70; H, 2.92; N, 58.70.

2.2 Characterization

X-ray intensity data for **1** were collected at 296 K on a MAR345 image plate using MoKα radiation (λ = 0.71073Å). Powder X-ray diffraction (PXRD) measurements were conducted on an X-ray diffractometer with Cu Kα (λ = 1.5406 Å) radiation (Siemens, Siemens/Bruker D5000, USA). UV–DRS were measured using a spectrophotometer (Shimadzu, UV3600 Plus, Japan). FTIR characterizations were performed with an Equinox 55 FTIR spectroscopy with an ATR modulus and an MCT detector. (Bruker, USA). The elemental composition of the samples was investigated using an elemental analysis (ThermoFisher, Flash EA 1112 Series, USA). Thermogravimetric (TGA)

analysis was performed through the Mettler Toledo with TGA/SDTA 851e. Nuclear magnetic resonance (NMR) spectra were recorded with a Bruker Avance II 300 MHz instrument from USA. TVB-N were measured by a Kjeldahl device (C. Gerhardt GmbH & Co. KG, C., Germany). Mass spectra (MS) were recorded using a Q-Exactive Thermo Fisher spectrometer. Magnetic susceptibilities were measured on a Quantum design MPMS-5 s SQUID magnetometer. ^{57}Fe Mössbauer spectra were recorded in transmission geometry with a constant acceleration mode Wissel spectrometer equipped with a 50 mCi ^{57}Co(Rh) source from Cyclotron Ltd and a Reuter Stokes proportional counter. The imaging of the vapochromic behavior of the sensor kept under analyte vapors were performed with a Colour Name Software (iPhone XR). NH_3 detection was performed with a smart sensor (Handheld Ammonia Gas NH_3 Detector Meter Tester Monitor Range 0-100 ppm Sound Light Alarm Gas Analyzers AR8500). whereas accurate water determination was realized with a H-B Instrument™ Durac™ Electronic Thermometer-Hygrometers designed with waterproof temperature probe. (More information in S3)

2.3 Sensor fabrication

The sensitivity experiments were conducted with a home-made 26 L seal chamber (Scheme S2). Firstly, $NH_3 \cdot H_2O$ was injected to the chamber with a syringe. Then, $NH_3 \cdot H_2O$ was evaporated to gaseous ammonia ($NH_{3(g)}$) by heating. Next, **1** was exposed to ammonia at different concentrations. The concentration in ppm was calculated with Eq. (1):[41]

$$C(ppm) = \left(\frac{10\ CRTd_v V_{injected}}{PM_w V_{chamber}}\right) \quad \textbf{(1)}$$

where *C(ppm)* is concentration of ammonia in *ppm*, *C* (wt%) is liquid concentration, *R* is the gas constant, *T* (K) is the temperature in absolute scale, d_v is the liquid mass density (g/cm^3), $V_{injected}$ is the injected volume in μL, *P* (atm) is the pressure inside the chamber, M_w is the molar mass of the liquid (g/mol), $V_{chamber}$ is the volume of chamber of 26L. The gas sensing experiments were carried out at room temperature (298 K). The imaging of the vapochromic behavior of the sensor kept under analyte vapors was

performed with a Colour Name Software (iPhone XR).

2.4 Raw data process and database analysis

Analyte response was calculated from the differences between the observed RGB1 (red, green, blue) and HSB2 (hues, saturation, brightness) values (color scale, 0−255) for the sensor before and after exposure to hazardous gases at room temperature. The Euclidean distance (Ed) corresponds to the total length of the 6-dimensional color vectors. To compare quantitatively the selectivity of the sensor among different analytes, the 6-dimensional Euclidean distances of the feature vectors are calculated for each pair of the examined analytes in the feature space using Eq. (2):[42]

$$Ed = \sqrt{(R - R_0)^2 + (G - G_0)^2 + (B1 - B1_0)^2 + (H - H_0)^2 + (S - S_0)^2 + (B2 - B2_0)^2} \quad \textbf{(2)}$$

Where values of *R, G, B1, H, S, B2* are color information of sensor to different analytes and R_0, G_0, $B1_0$, H_0, S_0, $B2_0$ are color information of sensor to the control. Two unsupervised statistical methods (principle component analysis (PCA) and hierarchical cluster analysis (HCA)), were performed for database clustering using RStudio (RStudio 4.1.0) and Origin (Origin Pro 2021) softwares, respectively; in all cases, minimum variance (i.e., "Ward's Method") was used for HCA clustering. For quantitative cross-validation, predictive classification was carried out using the support vector machine (SVM) analysis with Python, using a linear kernel with default parameters.[24]

The limits of detection (LODs) for relevant ammonia were determined according to Suslick *et al.*[43], from multipoint data by plotting LOD = 3**N**[A]/($S_A - S_C$) *vs.* concentration (in ppm), where [A] is the analyte concentration in ppm, *N* is the noise determined from multiple images of the sensor (noise was defined as the standard deviation among the controls (i.e., $N = \Sigma_n(\text{Ed}_{\text{control-n}} - \text{Ed}_{\text{control-avg}})^2/(n-1)$), S_A is the Euclidean distance (Ed) of the sensor after exposure to analytes, and S_C is the Ed of sensor to the control. A first-order polynomial fit was used to determine the LOD as [A] approached the LOD. Alternatively, one may extrapolate LOD from a single data point by simply taking the observed Ed value of the most responsive sensor after

exposure at 0.3 ppm concentration and dividing that into three times the noise observed for the sensor in a control experiment.

2.5 Determination of TVB-N

TVB-N content in chicken meat samples were measured by the Kjeldahl method. [44] (More information in S5)

2.6. Colorimetric sensor for real-time monitoring of food spoilage.

30g meat samples were placed in a sealed 1.5 L bottle to accumulate ammonia prior to freshness measurements. (The experimental details are in meat storage and sampling protocol of Scheme S3).

3. Results and discussion

3.1 Characterization

3.1.1 Crystal structure of 1

Single crystal X-ray diffraction analysis show that **1** crystallizes as colorless blocks (0.25x 0.1x 0.18 mm^3) in the octahedral space group $P2_1/c$ with a density of 1.923 cm^{-3} at 296 K. All of the plane positions are occupied by N atoms of two bidentate **Hbta** ligands (Fe(1) — N3 = 2.14(3) Å and Fe(1) —N13 = 2.23(3) Å), these distances are characteristic of high-spin (HS) Fe(II), and the *b*-axis position is occupied by the O atoms of two H_2O molecules (Fe(1) — O3 = 2.12(3) Å). Furthermore, two lattice water molecules were detected (Fig. 1a). The network structure of mononuclear complexes of **1** is connected by π-π* stacking between aromatic rings of **Hbta** (Fig. 1b) and H-bonding between the crystal water to form a 3D supramolecular network structure (Fig. 1c). As a consequence, no channels were detected (Fig. 1d) and therefore no pathway is available for vapor guest diffusion in the crystal lattice of this complex. Detailed crystallographic information is given in Table S1.

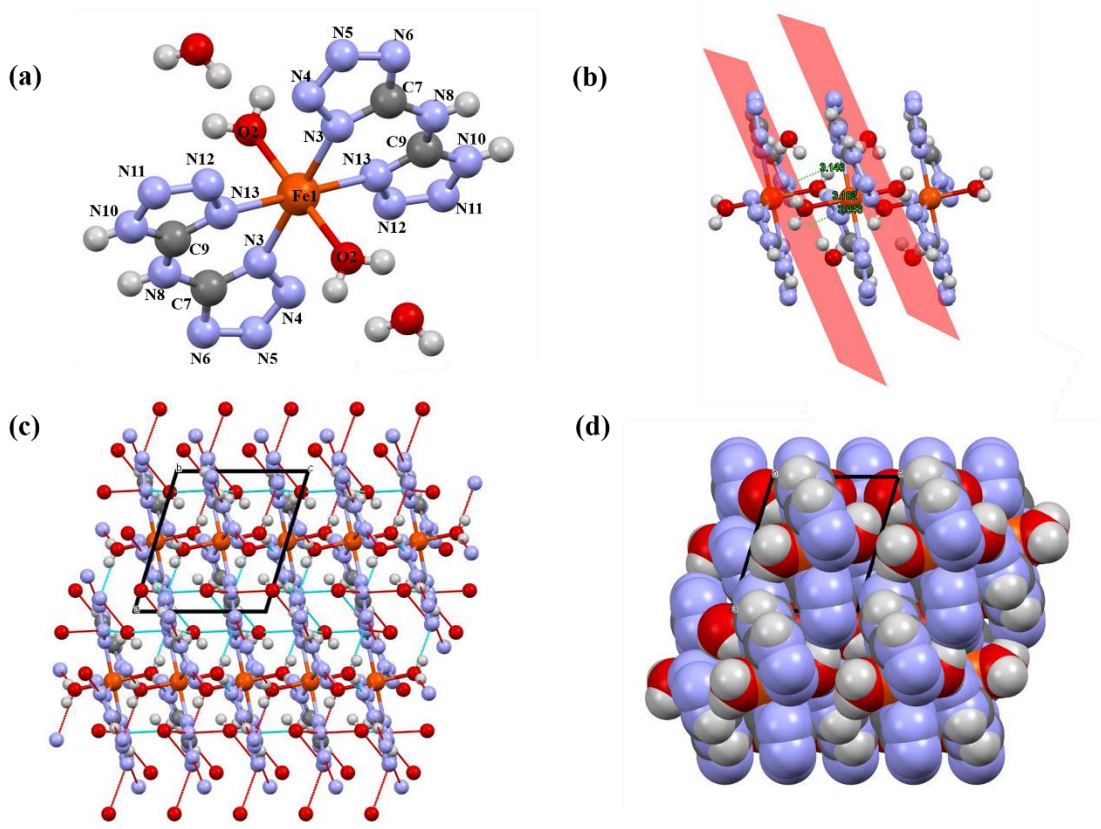

Fig. 1. Crystal structure of **1**: (a) Molecular unit of **1**. Part of the ordered carbon atoms from **Hbta**$^-$ group were omitted for the sake of clarity (color codes: dark grey: carbon; red: oxygen; blue: nitrogen, grey: hydrogen and orange: iron). (Fe(1) —N3 = 2.14(3), Fe(1) —N13 = 2.23(3) and Fe(1) — O3 =2.12(3) Å; ∠N13 − Fe1− N3 = 79.70(13), ∠N13 − Fe1−O2 = 88.82(13) and ∠N3 −Fe1−O2 = 92.33(14)). (b) π-π* stacking interaction of **1**. (c) Details of the crystal packing of **1** along the *b* crystallographic axis, show the network of H-bonding involving the oxygen and nitrogen atoms from H_2O and **Hbta** groups, respectively. Short N–H···O and O–H···N contacts along the *b*-axis. (d) Space-filling model as viewed down the *b*-axis, shows lack of channels and pores in **1**.

3.1.2 Stability analysis of 1

The thermal stability of **1** was analyzed by TGA/DTA (Fig. 2) and derivative of TGA (Fig.S1a). An endothermic mass loss was observed below 180 ºC due to dehydration. Furthermore, the anionic form of the coordinated ligand **Hbta** decomposes with an abrupt mass loss around 200 °C accompanied by an intense exothermic effect. Therefore, the structure of the sensor is stable below 150 ºC, thus delineating its operation conditions.

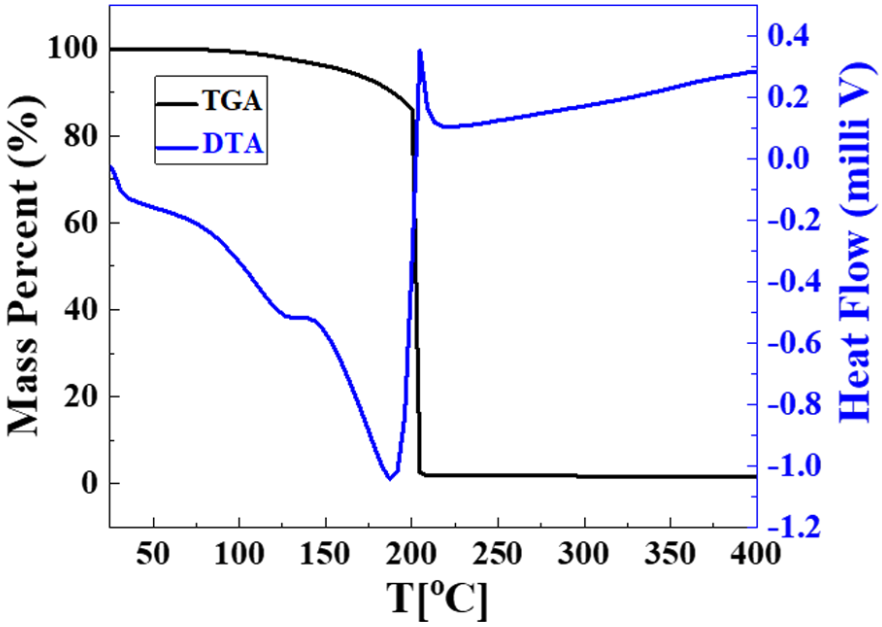

Fig. 2. TGA and DTA plots of **1** the range 25-400 °C.

In order to demonstrate the ability of **1** to discriminate among different vapor analytes, the sensor responses were determined for a series of different volatile molecules representing common organic functionalities at room temperature. (Fig. 3). Especially, after adsorption gas-phase molecules with amino groups, some of it turns from white/colorless to dark blue (1,2-diaminopropane), jet (isobutylamine), raw umber (furfurylamine), deep taupe (ammonia), liver (diethylamine), and outer space (ethylenediamine) colors. Excellent discrimination among these analytes is observed even without any chemometric manipulation. This is because liquid analytes are vaporized in air and subsequently diffuse into the surface of the Fe(II) complex leading to a partial spin state change of Fe(II) ions from HS to low-spin (LS) after adsorbing analytes. In addition, **1** has a great and fast response to some analytes with amines, as we shall describe later in Fig. 9. We have systematically investigated the effect of water molecules on our colorimetric sensor at different set values of humidity to assess whether the colorimetric response is reliable over the full range of humidity values that might be encountered in the real world. This also applied to $NH_{3(g)}$ at 5% and 50% (Fig. S1b). As a result, no color change was observed, indicating that our sensor is insensitive to water molecules.

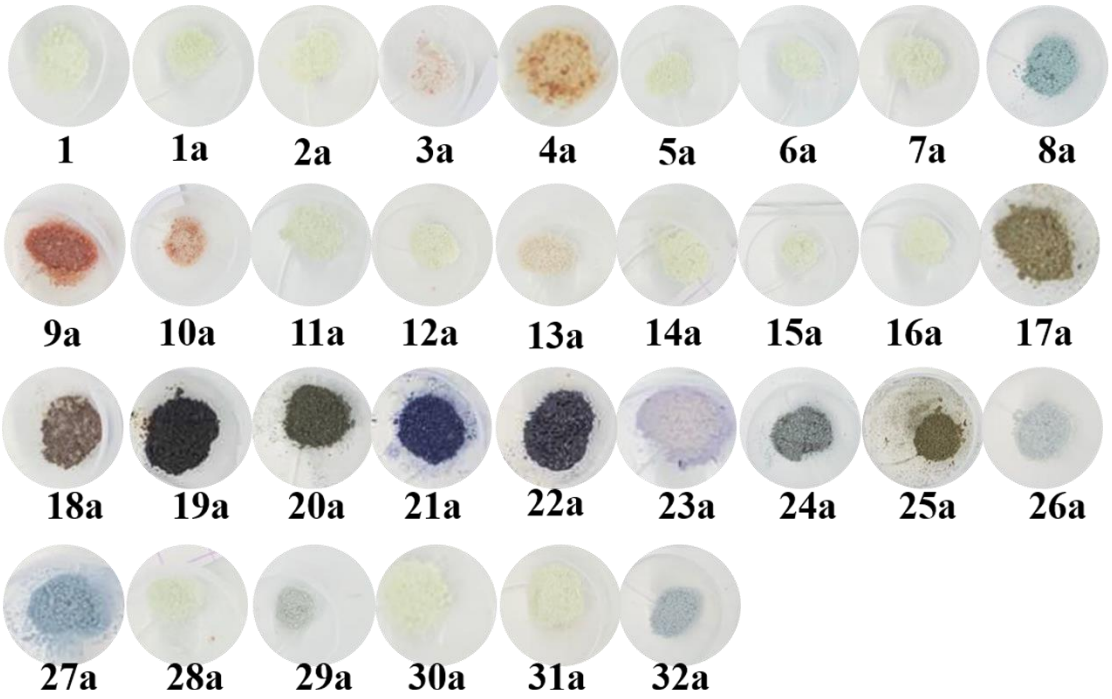

Fig. 3. Colorimetric sensor responses for 32 common analytes at saturation vapor pressure at room temperature.**1a** = H_2O; **2a** = acetonitrile; **3a** = formaldehyde; **4a** = dichloromethane; **5a** = chloroform; **6a** = acetone; **7a** = tetrahydrofuran; **8a** = pyridine; **9a** = MeOH; **10a** = ethanol; **11a** = 1-butanol; **12a** = 1-pentanol; **13a** = hydrochloric acid; **14a** = hydrogen bromide; **15a** = acetic acid; **16a** = sulfuric acid; **17a** = nitric acid; **18a** = NH_3; **19a** = isobutylamine; **20a** = diethylamine; **21a** = 1,2-diaminopropane; **22a** = ethylenediamine; **23a** = N_2H_4; **24a** = diethylenetriamine; **25a** = furfurylamine; **26a** = hexylamine; **27a** = triethylamine; **28a** = aniline; **29a** = 3-picolylamine; **30a** = 2-(trifluoromethyl)aniline; **31a** = 2-chloroaniline; **32a** = 1,2-diaminocyclohexane.

3.1.3 Ultraviolet−Visible Diffuse Reflectance Spectroscopy (DRS) analysis.

UV−Vis diffuse reflectance spectra (UV-DRS) were recorded on **1** before and after adsorption of selected analytes (Fig. 4 and Fig. S4). For **1**, a band is observed at λ = 240 nm, which can be assigned to a ligand-centered π−π* transition. [45] However, new peaks appear in the spectrum of **1** after adsorbing analytes with amine groups (in Fig. 4 and Fig. S4), which show high intensity bands in the UV region and broad transitions in the near-visible region. In the case of **1**@ethylenediamine, a band is observed at λ = 350 nm along with a broad band at λ = 570 nm. These are attributed to *n*-π* and d−d transitions of LS component ($^1A_1 \rightarrow {}^1T_1$),[37] respectively. Other

analogues display similar spectra with weaker bands except for **1**@NH_3 (Fig. 4 and Fig. S4). The presence of LS Fe(II) ions will also be confirmed by ^{57}Fe Mössbauer spectroscopy (see next section).

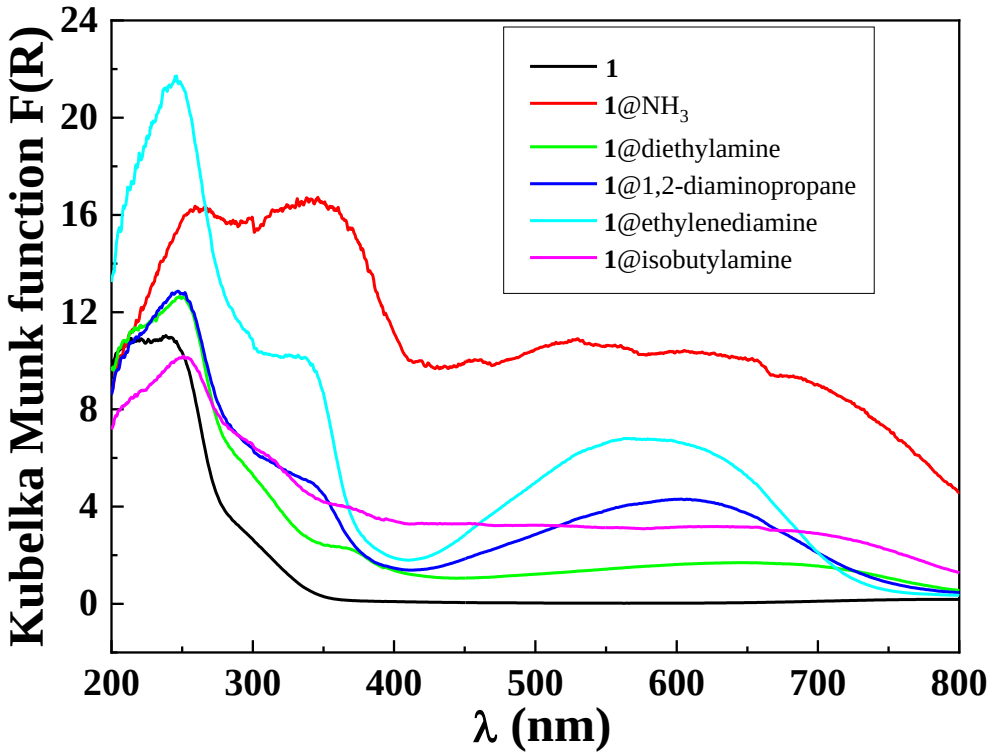

Fig. 4. Ultraviolet−Visible Diffuse Reflectance Spectroscopy (DRS) of **1** before and after the detection of hazardous gases with amino groups.

3.1.4 Mössbauer spectroscopy analysis

The spin state of **1** after hazardous gases absorption was confirmed by ^{57}Fe Mössbauer spectroscopy measurements carried out at room temperature in transmission mode (Table S2 and Fig. 5). At room temperature, the spectrum of **1** shows a quadrupole doublet which was fitted by Lorentzian lines to yield to isomer shift δ = 1.10(2) mm/s and quadrupole splitting ΔE_Q = 3.78(3) mm/s. Such parameters are typical for octahedral Fe(II) ions in the HS state (Fig. 5a).[37,38,46] This result agrees well with the magnetic susceptibility measurement which shows 100% of HS Fe(II) ions at room temperature (Fig. 6). A dissymmetry of the lines is observed, presumably due to a texture effect. LS Fe(II) ions were detected as a result of a partial spin state change from HS to LS after adsorbing hazardous gases with amines. For instance, **1**@NH_3

displays four quadrupole doublets assigned to two HS Fe^{II} ions (HS1 Fe^{II} and HS2 Fe^{II}) (area fraction = 14 and 10%; δ = 0.89(2) and 1.18(9) mms^{-1}; ΔE_Q = 3.42(5) and 2.00(2) mms^{-1}, respectively, red and pink spectra) and a LS Fe^{II} (area fraction = 41%; δ = 0.25(2) mms^{-1}; ΔE_Q = 0.78(8) mms^{-1} at room temperature, light blue spectra), as well as a LS Fe^{III} (area fraction = 35%; δ = 0.20(2) mms^{-1}; ΔE_Q = 1.49(6) mms^{-1} at room temperature, navy blue spectra) (in Fig.5b). For **1**@isobutylamine in Fig.5c, three quadrupole doublets attributed to LS-Fe^{II} (area fraction = 24 %; δ = 0.22(5) mms^{-1}; ΔE_Q = 0.57(8) mms^{-1}, light blue spectra), HS-Fe^{II} (area fraction = 35%; δ = 1.10(9) mms^{-1}; ΔE_Q = 3.78(2) mms^{-1}, red spectra) and LS-Fe^{III} (area fraction = 41%; δ = 0.15(3) mms^{-1}; ΔE_Q = 1.53(5) mms^{-1}, navy blue spectra) are observed at room temperature. These parameters (light blue spectra) are characteristic of LS Fe^{II} ions in a FeN_6 core, due to oxygen atoms replace by nitrogen atoms to coordinate with Fe(II) after amines (ammonia) adsorption.[38] Other analogue display similar LS-Fe^{II} spectra in Fig. 5 and Fig. S5. After adsorbing the gas-phase molecules with amino groups, which may form different interactions with the central atom and surface molecules, a new spin state is generated. Such result is confirmed by magnetic measurements (see next section).

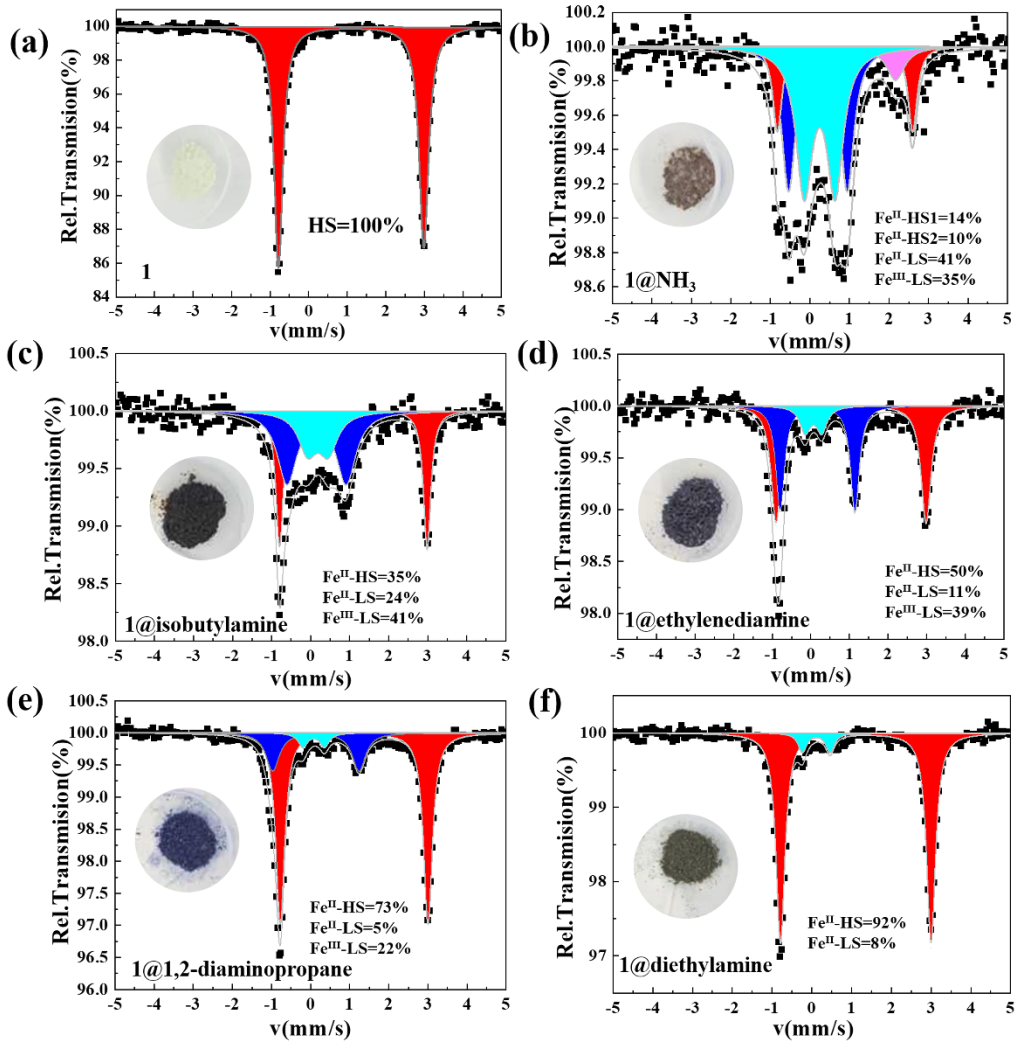

Fig. 5. Mössbauer spectra of **1** before and after the detection of hazardous gases with amino groups at room temperature.

3.1.5 Magnetic properties analysis

The magnetic properties of **1** before and after contacting analytes, have been studied over the temperature range of 4-400 K with a SQUID and are displayed in the form of χT *vs*. T, χ being the molar magnetic susceptibility (Fig. 6 and Fig. S6). At 298K, χT = 3.35 $cm^3mol^{-1}K$ which corresponds to the expected value for HS Fe(II) ions. Compare with **1**, the χT curve of **1** after adsorbing hazardous gases of amines is reduced to various degree. For **1**@NH_3, **1**@ethylenediamine and **1**@isobutylamine, χT obviously decreases and drops rapidly reaching a value of 1.34, 1.77 and 1.50 $cm^3mol^{-1}K$, respectively, at room temperature. The results indicate that the partial spin state change from HS to LS due to adsorbed analytes with amino groups molecules results

in the increase of the ligand field strength of **1** at room temperature. This is in very good agreement with ^{57}Fe Mössbauer spectroscopy results (See previous section).

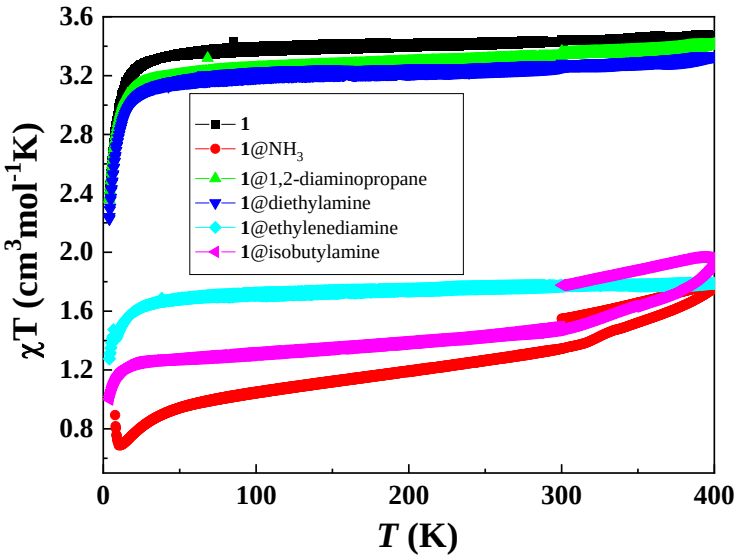

Fig. 6. χT *vs* T curves for **1** before and after adsorbing hazardous gases in the temperature range of 4-400 K.

3.2 Chemosensing properties of 1 containing various hazardous gases

3.2.1 Selectivity for hazardous gases

Interestingly, the images photographed using a smartphone camera were converted into digital information to afford RGB1 (red, green, blue) and HSB2 (hues, saturation, brightness) values by a conventional application (Color Name AR), to examine the multivariate distances (Euclidean Distance) between the analyte responses in 6-dimension.[38] In order to measure the difference between two colors, the difference is assigned to a distance within the color space.[24] Simple comparisons of the spatial distances in their full original vector space between an observed color and a pre-collected library were extremely rapid. RGB1 and HSB2 color space, a hierarchical cluster analysis (HCA) was performed. Such analysis makes use of only digital data representing the observed difference colors without considering any chemical information.[47] According to the set of colors observed in Fig.3 ranging from blue, reddish, white, green, one can assume that samples can be categorized in three or four different groups (depending on their colors). For a more detailed determination of color

dissimilarity between samples, data were subjected to HCA. HCA is a multivariate-statistics that enable to determine clusters of observations within a data set.[48,49] HCA was performed to generate dendrograms (Fig. 7), for the cluster analysis using Ward's algorithm.[50]

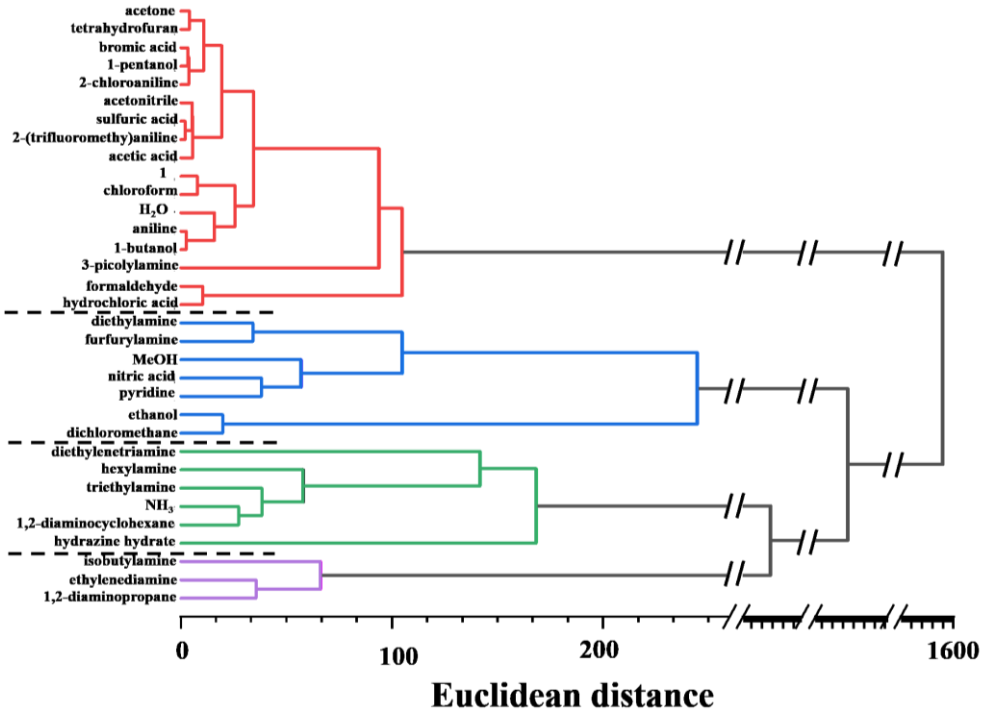

Fig. 7. HCA dendrogram of **1** (colorimetric detection tree diagram) of 32 analytes at saturation vapor pressure showing the relative relationship between gas analytes at room temperature. Averages of 3 trials were used for each analyte. The sorting of the analyte was classified due to the characteristics of RGB1 and HSB2 values in Table S3.

Analytes with amino groups gas-phase samples are accurately identified against each other by HCA. Principal component analysis (PCA) is a technique for reducing the dimensionality of such datasets, increasing interpretability but at the same time minimizing information loss.[24] The PCA score plot based on the first two principal components (PC1 and PC2) displays a similar pattern of clustering results as compared to HCA, with four clusters identified, with no overlap among clusters (Figure 8a). The scree plot (Figure 8b) shows that 2 dimensions are needed to account for >98% of the total variance of the data, which means that the sensor offers a wide range of detection

capabilities. Remarkably, an excellent differentiation of closely related analytes was achieved with the data shown in Table S3.

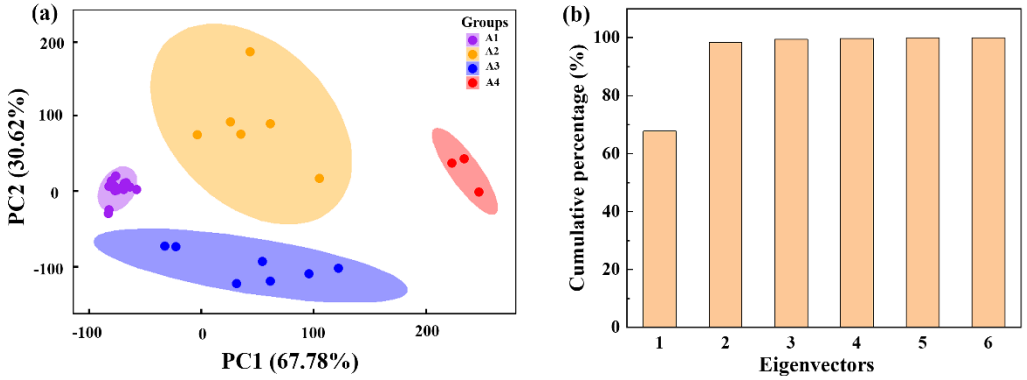

Fig. 8. (a) 2D score plot of PCA results of sensor **1** to 32 analytes. (b) Scree plot of all analytes. Averages of 3 trials were used for each analyte. The sorting of the analyte was classified due to the characteristics of RGB_2 and HSB_2 values in Table S3. (**A1**: acetone, acetonitrile, bromic acid, sulfuric acid, **1** (control), 1-pentanol, H_2O, formaldehyde, 2-chloroaniline, aniline, 1-butanol, hydrochloric acid, chloroform, acetic acid, 2-(trifluoromethyl)aniline, 3-picolylamine, tetrahydrofuran; **A2**: hydrazine hydrate, 1,2-diaminocyclohexane, ammonia, triethylamine, hexylamine, diethylenetriamine, ; **A3**: diethylamine, methanol, furfurylamine, ethanol, nitric acid, dichloromethane, pyridine; **A4**:1,2-diaminopropane, ethylenediamine, isobutylamine).

The speed of discoloration is another crucial factor for the detection of analytes by any reliable sensor. From this perspective, the correlation of Euclidean distance (Ed) with different contact time from 0 to 2h was investigated. Fig. 9 shows that Ed increased rapidly during the first 10 min, which is mainly because that the detection sites of the sensor are abundant at the beginning. As the detection continues, both number of vacant sites and analytes concentration gradient decrease, resulting in the decrease in the speed of discoloration. Finally, the Ed saturates at a maximum value, indicating that adsorption detection reaches equilibrium. Thereby, 10 min of contact time was enough for the detection of analytes at room temperature. In addition, among them, fast and obvious colors change were observed for NH_3, 1,2-diaminopropane, isobutylamine, ethylenediamine (Fig.9). Furthermore, it demonstrates that **1** can quickly detect several toxic gases with amino groups at room temperature (Table S4).

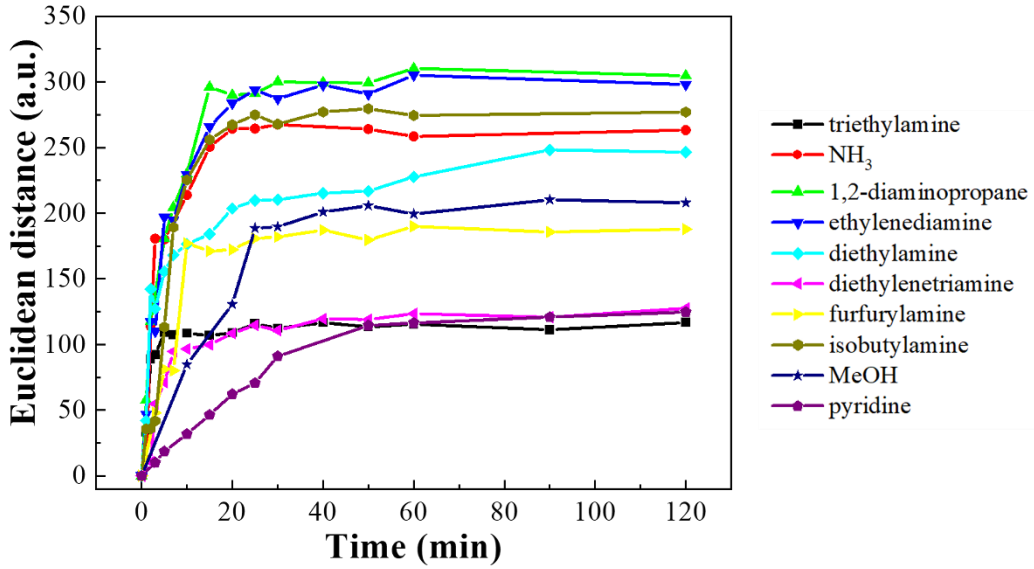

Fig. 9. Euclidean distance *vs.* time for 10 representative analytes at statured concentrations; All experiments were performed in triplicate. The Euclidean distance corresponds to the total length of the 6-dimensional color vector shown in Table S4.

3.2.2 Sensitivity for $NH_{3(g)}$

As the concentration of $NH_{3(g)}$ increases from 0 to 142 ppm, the color of our sensor changes from pastel gray to pastel blue, which can be distinguished by the naked eyes directly at room temperature, as shown by the plot of the Ed and the concentration (Fig. 10a). The Ed value increases sharply from 0.5 to 5.7 ppm, after the Ed value slowly increases up to 140. Data was fitted best using an exponential type function with very good determination coefficients (R^2 = 0.99 for $NH_{3(g)}$) (Fig.10a). Most interestingly, this curve can be helpful not only to predict concentration of ammonia (< 3 ppm) by evaluating the color of our sensor, but also to evaluate the risks of ammonia in the environment (with concentration > 3 ppm). The calibration curve (Fig. 10b), displays LODs at low ppb level. An excellent linearity is observed with $R^2 > 0.99$ for $NH_{3(g)}$. The sensor response at extrapolated LOD was recollected (105 ppb) in Fig.S7. A comparison of LODs calculated by these two methods gives very similar results (Table S6). The PCA score plot based on the first two principal components displays a pattern of clustering results with no overlap among clusters (Fig. S8a). The scree plot (Fig. S8b) shows that 2 dimensions are needed to account for > 99% of the total variance of the data, which means that the sensor has a wide range of detection $NH_{3(g)}$ concentration

capabilities. For comparison, SVM analysis offers supervised and more quantitative method for data classification and predication. The results of SVM analysis using a standard leave-one-out permutation model are shown in Table S7. All concentrations of ammonia show grouping results with 100% classification accuracy. This outcome demonstrates that the performance of our sensor is superior to that in the previously reported method for the detection of $NH_{3(g)}$ at room temperature. According to the data of the National Institute for Occupational Safety and Health (NIOSH), employers can only be exposed to working environment where the concentration of $NH_{3(g)}$ is lower than 25 ppm. [51] Therefore, our sensing system shows great potential for applications in daily life given it holds a much lower detection limit of 105 ppb for $NH_{3(g)}$.

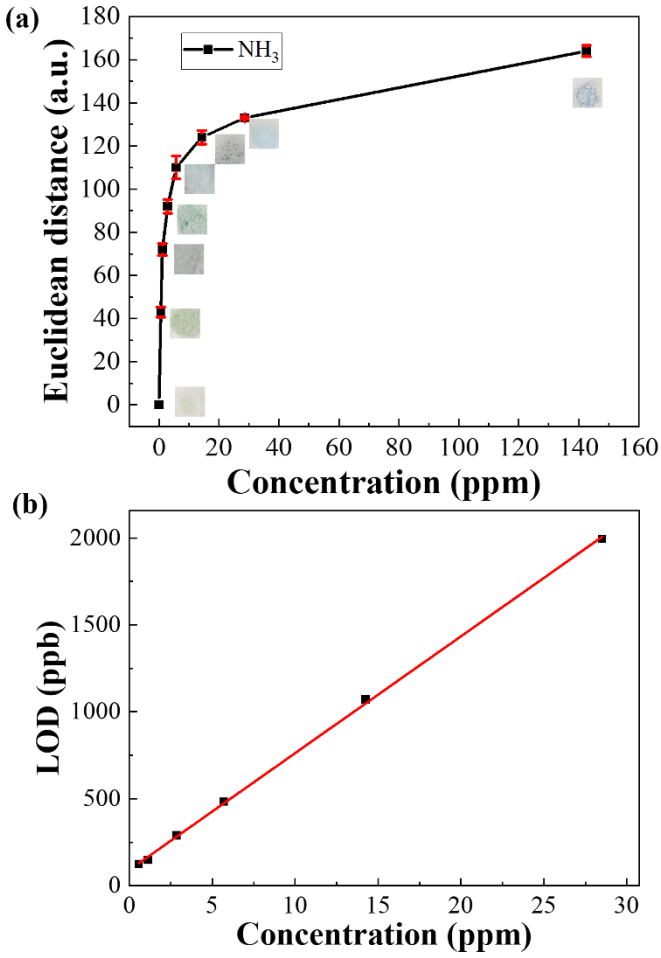

Fig. 10. (a) Sensor response to $NH_{3(g)}$ at different concentration. Relation curve between the Euclidean distance and the concentration of the $NH_{3(g)}$ and effect of initial concentration of $NH_{3(g)}$ on color changing of **1** at room temperature. The ratio of Euclidean distance *vs* $NH_{3(g)}$ concentration in the range of 0 to 140 ppm. (When the data were examined, a linear response was obtained for a concentration lower than 3 ppm while curve slowly saturates above 3 ppm.)

The Euclidean distance corresponds to the total length of the 6-dimensional color vector shown in Table S5. (b) Calibration curve for LODs of $NH_{3(g)}$ (Details are gathered in Table S6).

3.2.3 Regeneration of colorimetric sensor

Although meat monitoring does not necessarily require the regeneration of a sensor, such regeneration ability is still considered as an important factor for the potential application of a given colorimetric sensor. An excellent sensor must not only have a good response property but also good regeneration ability for the sensor to be economically gainful. In this study, two representative gases were selected, $NH_{3(g)}$ (which is not only released from food spoilage, but also is widely used in industry) and isobutylamine$_{(g)}$ (as a representative of organic amines to check if aliphatic amines would present regenerative property). Desorption experiments were performed by using a HCl solution (4%) as eluent. As shown in Fig. 11, the removal efficiency of the sensor in each regeneration cycle, indicates that **1** can be reused up to 8-10 times.

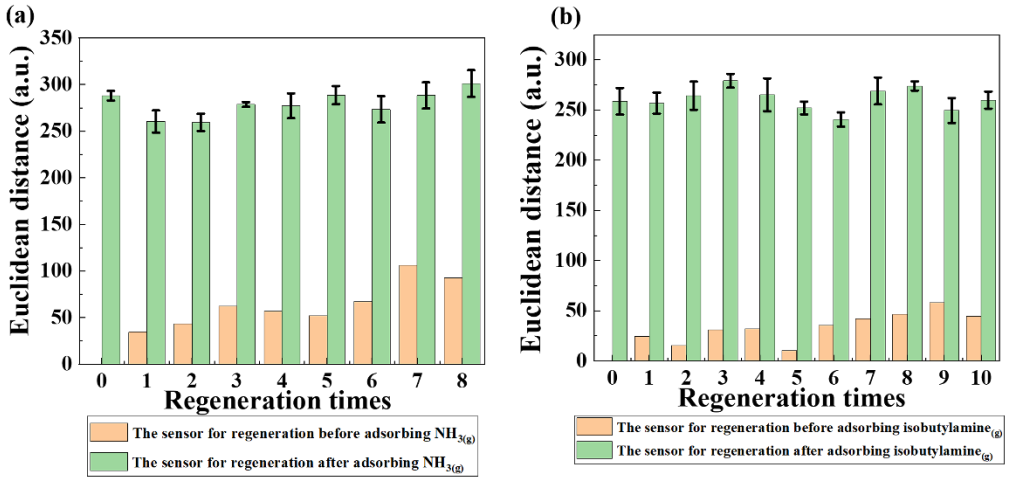

Fig. 11. Diagram of reusability test for the colorimetric sensor on the regenerated at room temperature. All experiments were performed in triplicate. The Euclidean distance corresponds to the total length of the 6-dimensional color vector shown in Table S8.

Comparison of the detection and sensing performances of $NH_{3(g)}$ and aliphatic amines of different materials to **1** is given in Table 1. Traditional sensing materials such as nanoparticles,[52] metal oxide semiconductor and quartz crystal microbalance,[53] etc., have been reported. Although sensors based on metal oxide semiconductors [52] or metal imidazolate framework materials [54] have a simple structure and are low cost,

their operating temperature is too high (>75ºC) to compete with our complex which operates at room temperature. For sensors based on a quartz crystal microbalance, the sensing process is based on the principle of similar polarity, thus giving a low selectivity. In addition, such equipment is not user friendly at all, and needs to be carefully maintained, in contrast to our complex. Compared with traditional sensors, **1** has the advantage to show a high selectivity (with a lower detection limit of 105 ppb for $NH_{3(g)}$), simple to operate, environmentally friendly, in-situ, real-time and low-cost for detecting $NH_{3(g)}$. Importantly, **1** can excellently respond to broadly hazardous gases with amino groups, and produce obvious color changes that can be seen by the naked eyes at room temperature. Most importantly, our complex can not only discriminate $NH_{3(g)}$ from mixed toxic gases (discriminate primary amines from aromatic amines) (Fig. S9 and Table S9) but also evaluate $NH_{3(g)}$ concentrations at very low levels (ppb).

Table 1 Comparison of the detection $NH_{3(g)}$ and aliphatic $amines_{(g)}$ sensing performances of different materials.

Sensor	Analyte(g)	LODs (ppb)	Response (min)	t (ºC)	Mechanism	Ref.
1	1,2-diaminopropane ethylenediamine isobutylamine NH_3	--- --- --- 105	< 10	r.t.	From HS FeN_4O_2 to LS FeN_6 core and H-bonding	This work
MAF	NH_3	10^3	5	r.t.	DASAs	[55]
PtNP/a-IGZO	NH_3	10^3	---	250	ISSASCA	[52]
Calixarene functionalized SWCNT	NH_3	600	15	r.t.	EGE	[56]
VODFON	diethylamine	10^5	0.03	350	SIA	[57]
Polymerized castor oil based QCM	NH_3	397	---	R.T.	H- bonding	[53]
dyes	isobutylamine	$5x10^3$	10	r.t.	BLABT	[58]
NCP	ethylenediamine	$5.6x10^3$	---	r.t.	ICTC	[59]
PR	ethylenediamine	1070	---	r.t.	H-bonding	[60]
Co-MOF-1	isobutylamine	---	>60	r.t.	ET	[61]

MAF : Meldrum's activated furan; DASAs : donor–acceptor stenhouse adducts; platinum nanoparticle /amorphous In-Ga-Zn-O= Pt NP/a-IGZO; ISSASCA : increased specific surface area and superior catalytic activity of the Pt NPs; SWCNT : single-walled carbon nanotubes; EGE : electrostatic gating effect; VODFON: V_2O_5-decorated α-Fe_2O_3 nanorods; SIA : sensors interact with amines; QCM: quartz crystal microbalance; BLABT : Brønsted-Lowry acid base theory; NCP : nitrated conjugated polymer; ICTC : intermolecular charge transfer complex; PR:N,N′-bis(2-(trimethylam-moniumethylene) per-ylene-3,4,9,10-tetracarboxyldiimide-(R)-(-)-camphorsulfonic acid salt; ET: electron transfer.

3.3 Discoloration mechanism of 1 containing various analytes vapors

Based on the above results, a discoloration mechanism of **1** towards $NH_{3(g)}$ and analytes with amino groups at room temperature was proposed (Fig. 12). A reasonable and persuasive explanation for this discoloration is that Fe(II) ions on the surface of the sensor are coordinated with analytes molecules with NH_2- groups, replacing

coordinated O atoms. As shown in this work (Fig.5 and Fig.6), LS state of **1** appears, due to a partial spin state change from HS FeN_4O_2 to LS FeN_6 after adsorbing analytes with amines or NH_3. In addition, since the electronegativity and the radius of the N atoms are smaller than the ones of the O atoms, rich-nitrogen ligands have a stronger ligand field, which leads to the formation of LS Fe(II) ions. Furthermore, the inevitable existence of hydrogen bonds in the coordination species of nitrogen-rich ligands, may promote color change of **1**.

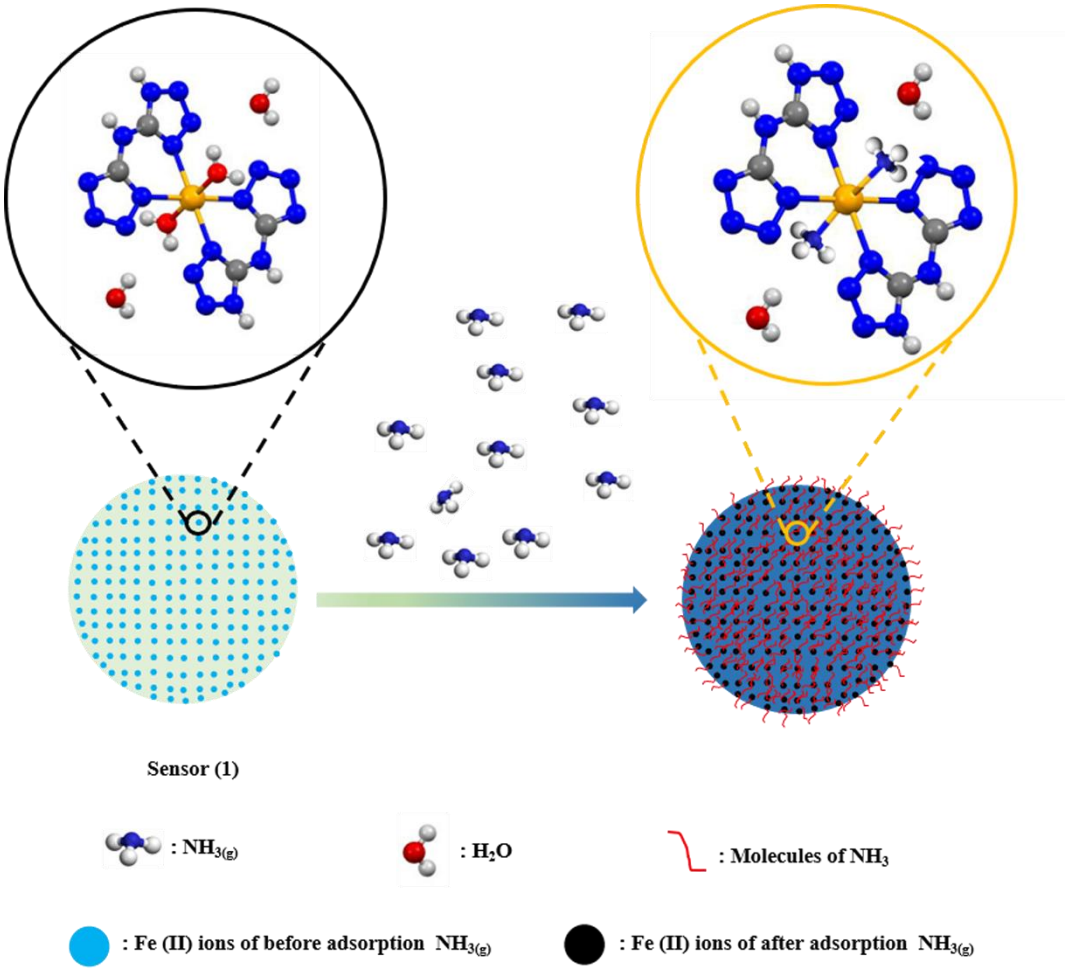

Fig. 12. Suggested discoloration mechanism of **1** containing various analytes vapors at room temperature. (color codes: dark grey: carbon; red: oxygen; blue: nitrogen, grey: hydrogen and orange: iron).

3. 4 Applications in the assessment of meat freshness

Ammonia has been used as an important indicator of food spoilage state. In order to verify the practical application property of our colorimetric sensor detection system, it was used to real-time and in-situ detect $NH_{3(g)}$ from meat samples and to evaluate meat freshness at room temperature (23 ± 1 °C). The response of **1** towards trimethylamine$_{(g)}$ and dimethyl sulfide$_{(g)}$, which are interference analytes during meat spoilage, can be ignored (Fig. S10). Euclidean distance-based in-situ monitoring of meat samples was then performed over time (Fig. 13a). Distance was shown to increase quickly after 24 h, especially for chicken meat, which indicates that the chicken spoilage rate is relatively fast, and the release of ammonia gas is relatively high too. The accurate concentration of ammonia vapor in the sample was measured using a smart ammonia gas detector (AR8500) as standard control (Fig. 13b). No ammonia release was observed before 24h at room temperature (23±1 °C) for meat of chicken (breast), pork (belly) and beef (steak) packs. However, the situation differs after 36 h with 3.6 ppm (for chicken), 0.2 ppm (for pork) and 0.2 ppm (for beef) level. At 48 h, 24.7 ppm were detected for chicken, 1.2 ppm for pork and 0.9 ppm for beef. (This result is consistent with the experimental result of **1** in Fig. 13a). To better reveal the complex system's capabilities to quantitatively assess meat freshness, HCA analyses was conducted on the database collected for spoilage of meat samples. HCA manifests the clustering of data with three distinct classes of responses, which means there are three processes of meat from fresh to spoilage, as shown in Fig. 13c. The cluster with the lowest response is the freshest meat, which was labeled "Fresher", which contains 0 h storage of three meats (as control), and from 12 h to 24 h storage of chicken, beef and pork (The result is consistent with Fig.13a and 13b, which shows there no ammonia gas release from meats from 0 h to 24 h). The middle response cluster, labeled "less fresh", contains 36 h storage of pork and beef meat as well as 48 h storage of beef (Ammonia release has been detected, but not much from 24 h to 48 h for pork and beef meat, in Fig.13a and 13b). The most responsive cluster, labeled "spoiled", including the 36 h storage of chicken, 48 h storage of chicken and pork, and 60 h storage of chicken, pork and beef meats (The release of ammonia is too high, but after 48 h, the release of

ammonia is relatively fast, in Fig.13a and 13b). The PCA score plot based on the first two principal components display a similar pattern of clustering results as compared to HCA with no overlap among clusters in Fig. S11. As with the previously discussed SVM analysis of the individual gas analytes, a leave-one-out permutation cross-validation gave perfect identification of all 16 classes (three meats at 5 times and the control) with an error rate of <1% (Table S13).

Since a number of volatile nitrogenous compounds are released during the spoilage process of high-protein foods, commonly referred as TVB-N, it is important to determine them to assess the freshness of meat.[4] For instance, a TVB-N $\leqslant$ 25.5 mg/l00 g (for chicken meat) is considered as an acceptable value for fresh meat.[62] When delivered from the supermarket, our fresh chicken batch showed a TVB-N = 14.16 mg/l00 g (Fig. S12). After only 1.4 days (34 h), TVB-N exceeded 25.5 mg/l00 g, indicating the beginning of meat spoilage, which continue to grow after two days, reaching unacceptable values after 5 days. Such result is consistent with the conclusion of our colorimetric sensor detection system (36h). The magnitude of overall response time of **1** to ammonia with the same storage duration at 23$\pm$1 ^{o}C follows the order: chicken > pork > beef. Such an order may be modified by differences in the protein compositions of three type of meats (different muscle types) and pre-slaughter conditions, and probably more importantly, by differences in the bacteria strains [63,64] and bacterial activities [65] that are growing on the meats during spoilage. The results suggest the potential practical applications of our colorimetric sensor to measure ammonia in daily life, e.g. for food packaging, and air quality monitoring. The performance of our sensor system against several disinfectants commonly used in the meat and fish packaging industry,[66] including chlorine and peracetic acid, was checked (Fig. S13). No effect was found showing the high resistance performances of our sensor. For a commercial use, the sensor would need to be protected against food contact, e.g. by embedding the sensor into silica gel to produce either particles which would be placed in a transparent bag in the food packaging, or a film which could be stuck on the food packaging itself.

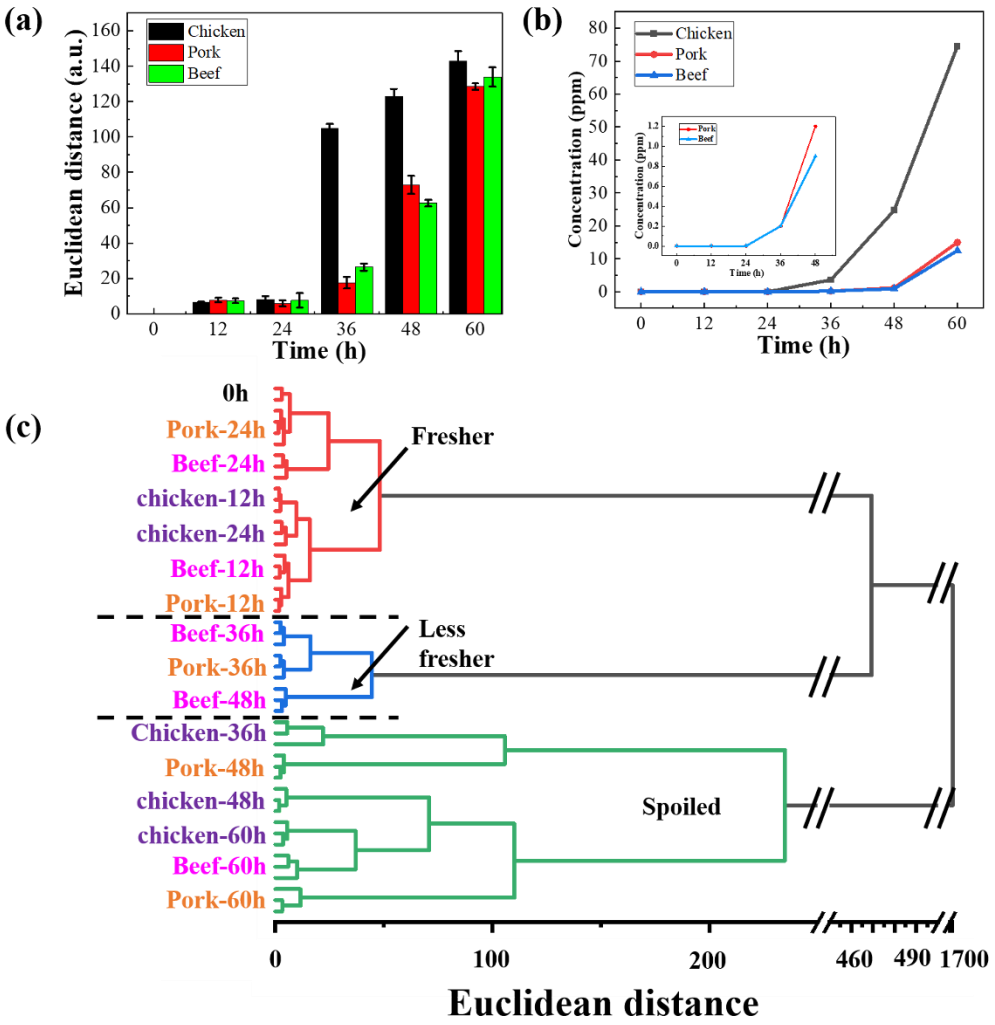

Fig. 13. (a) Response of **1** to three meat products stored at room temperature (23±1°C), (b) concentrations of ammonia were measured by ammonia gas detector from meat products at room temperature (23±1°C) (insert: Response of **1** to low concentration of ammonia), (c) dendrogram showing hierarchical cluster analysis of the spoilage of meat (chicken, beef and pork) at room temperature (23±1°C) with different time; All experiments were performed in triplicate. The Euclidean distance corresponds to the total length of the 6-dimensional color vector shown in Table S10.

3.5 Reproducibility of meat sample measurements

To assess the consistency of our colorimetric sensing method, a reproducibility study was conducted on three separately prepared colorimetric sensors (at one month interval), by comparing their response to chicken meat.[24] In addition, comparisons were made among three separate chicken batches bought at a day interval, which were

each tested with **1**.[24] For the study, chicken meat (30 g) was stored at room temperature for 48 h, and measurements were done in triplicate.

Reproducibility for the colorimetric sensing was evaluated from the average Euclidean distance from triplicate trials (Fig. S14 and Table S14). Three preparations of **1** afforded an Ed = 151±8 on single chicken batches. For comparison, the reproducibility of three chicken batches was tested too affording an Ed = 156+14. Combined with relative standard deviation (RSD), the differences in the batches of colorimetric sensors were found smaller compared to the differences among the chicken meat originating from separate purchases (Table S14).

Comparison of the ability to assess the freshness of meat by different sensor materials is shown in Table 2. At room temperature, small organic molecules released from spoiled meat can quench fluorescence of existing sensors.[22,67,68] Although this method is very effective, the measurement of fluorescence intensity is not widely available for public use due to price and professional technical factors, thus limiting any reliable application. On another ground, pH-sensitive films were applied to food packaging with color changes being detected by naked eyes.[69] However, since everyone has a different level of color perception by naked eye, such methods directly using the naked eye to identify whether the food is fresh or not, is obviously subjective and inaccurate. In contrast, our complex **1** combined with a smartphone is not only highly sensitive, powerless, low cost, but also can real-time and in-situ evaluate the freshness of meat, and is available to everyone with the simple use of a handy smartphone.

Table 2 Analysis and comparison of different sensor materials on real samples.

Sensor	Meat	T (°C)	Unsafe time (h)	Ref.
FN	chicken	25	>36	[22]
	pork	25	>36	
pH-sensitive films	chicken	30	>24	[69]
CSA	chicken			
	beef	25	>24	[65]
	pork			
1	pork	23±1	>24	
	chicken	23±1	>24	This work
	beef	23±1	>24	

FN: Fluorescent Nanotubes; CSA: Colorimetric Sensor Array.

4. Conclusions

In summary, a novel type and high-performance gas colorimetric material based on a nonporous Fe(II) complex was designed for quantitative detection of NH_3. It provides a real-time monitoring and in-situ assessment of meat freshness using a simple color recognition by smartphone. In addition, the colorimetric material can effectively discriminate hazardous gases with amino groups at room temperature and allows trace detection of ammonia (the detection limit is 105 ppb for $NH_{3(g)}$). The complex also features has an excellent regenerating ability too. The coloration mechanism involves a partial spin state change of Fe(II) ions after adsorption with an additional role of hydrogen bonding. Overall, such colorimetric material could provide broadly selectivity towards various hazardous gases with amino groups and high sensitivity to ammonia, opening up an opportunity to develop a new generation of room temperature portable electronic nose systems for real-time assessment and in-situ measurement of the freshness of meat, e.g. by inserting our sensor into food packaging, via processing a thin film.

CRediT authorship contribution statement

Li Sun: Methodology, Software, Investigation, Characterization, Writing–original draft. Aurelian Rotaru: Methodology, Software, Characterization. Yann Garcia: Supervision, Methodology, Software, Investigation, Writing–review & editing.

Declaration of Competing Interest The authors declare that they have no known competing financial interests or personal relationships that could have appeared to influence the work reported in this paper.

Acknowledgements

This work was supported through the Fonds De La Recherche Scientifique—FNRS (CDR 33694457, PDR T.0095.21), the Ministère de l'Education et de la Recherche de Roumanie and WBI. L. S. was supported by fellowship from the China Scholarship Council (201804910584). We thank to Dr. M. Chen for her input on the Hierarchical Cluster Analysis.

Appendix A. Supporting Information

The Supporting Information is available free of charge on the Elsevier publications website. Overview of FT-IR, Powder X-ray diffractograms, Diffuse-reflectance spectroscopy, ^{57}Fe Mössbauer spectroscopy parameters, Temperature-dependent χT plots, all data of Euclidean distance of **1** before and after adsorption of different guest molecules at room temperature, the influence of acids and different humidity on sensor properties and all data of applications in the assessment of meat (chicken, beef and pork) freshness by the colorimetric sensor.

References

[1] Ma, Z., Chen, P., Cheng, W., Yan, K., Pan, L., Shi, Y., Yu, G., 2018. Highly sensitive, printable nanostructured conductive polymer wireless sensor for food spoilage detection. Nano Lett. 18, 4570–4575.

[2] Nguyen, L.H., Naficy, S., McConchie, R., Dehghani, F., Chandrawati, R., 2019. Polydiacetylene-based sensors to detect food spoilage at low temperatures. J. Mater. Chem. C 7, 1919-1926.

[3] Mohammadi, Z., Jafari, S.M., 2020. Detection of food spoilage and adulteration by novel nanomaterial-based sensors. Adv. Colloid Interface Sci. 286, 102297.

[4] Cai, C., Mo, J., Lu, Y., Zhang, N., Wu, Z., Wang, S., Nie, S., 2021. Integration of a porous wood-based triboelectric nanogenerator and gas sensor for real-time wireless food-quality assessment. Nano Energy 83, 105833.

[5] Valdez, M., Gupta, S.K., Lozano, K., Mao, Y., 2019. ForceSpun polydiacetylene nanofibers as colorimetric sensor for food spoilage detection. Sens. Actuators B: Chem. 297, 126734.

[6] Zhang, D., Yu, S., Wang, X., Huang, J., Pan, W., Zhang, J., Meteku, B.E., Zeng, J., 2022. UV illumination-enhanced ultrasensitive ammonia gas sensor based on (001)TiO_2/MXene heterostructure for food spoilage detection. J. Hazard. Mater. 423, 127160.

[7] Matindoust, S., Farzi, A., Baghaei Nejad, M., Shahrokh Abadi, M.H., Zou, Z., Zheng, L.R., 2017. Ammonia gas sensor based on flexible polyaniline films for rapid detection of spoilage in protein-rich foods. J. Mater. Sci. Mater. Electron. 28, 7760-7768.

[8] Bekhit, A.E.D.A., Holman, B.W.B., Giteru, S.G., Hopkins, D.L., 2021. Total volatile basic nitrogen (TVB-N) and its role in meat spoilage: A review. Trends Food Sci. Technol. 109, 280-302.

[9] Sutthasupa, S., Padungkit, C., Suriyong, S., 2021. Colorimetric ammonia (NH_3)

sensor based on an alginate-methylcellulose blend hydrogel and the potential opportunity for the development of a minced pork spoilage indicator. Food Chem. 362, 130151.
[10] Jasuja, H., Peterson, G.W., Decoste, J.B., Browe, M.A., Walton, K.S., 2015. Evaluation of MOFs for air purification and air quality control applications: Ammonia removal from air. Chem. Eng. Sci. 124, 118-124.
[11] Ryer-Powder, J. E., 1991. Health effects of ammonia. Plant/operations prog. 10, 228-232.
[12] Yarandi, M.S., Mahdinia, M., Barazandeh, J., Soltanzadeh, A., 2021. Evaluation of the toxic effects of ammonia dispersion: consequence analysis of ammonia leakage in an industrial slaughterhouse. Med. Gas Res. 11, 24-29.
[13] Jafari, M.J., Matin, A.H., Rahmati, A., Azari, M.R., Omidi, L., Hosseini, S.S., Panahi, D., 2018. Experimental optimization of a spray tower for ammonia removal. Atmos. Pollut. Res. 9, 783-790.
[14] Dai, S., Prempeh, N., Liu, D., Fan, Y., Gu, M., Chang, Y., 2017. Cholesteric film of Cu(II)-doped cellulose nanocrystals for colorimetric sensing of ammonia gas. Carbohydr. Polym. 174, 531-539.
[15] Krishnan, S.T., Son, K.H., Kim, N., Viswanath, B., Kim, S., An, J.H., 2017. Development of simple and sensitive hydrogel based colorimetric sensor array for the real-time quantification of gaseous ammonia. Mater. Sci. Eng. C 72, 583-589.
[16] Wang, Q., Lonergan, S.M., Yu, C., 2012. Rapid determination of pork sensory quality using Raman spectroscopy. Meat Sci. 91, 232-239.
[17] Papadopoulou, O., Panagou, E.Z., Tassou, C.C., Nychas, G.J.E., 2011. Contribution of Fourier transform infrared (FTIR) spectroscopy data on the quantitative determination of minced pork meat spoilage. Int. Food Res. J. 44, 3264-3271.
[18] Anusankari, S., Balaji Ganesh, A., Subasri, R., Deepa, N., 2019. Optical determination of carbon dioxide and oxygen by a fluorescent membrane to evaluate the freshness of meat products. Instrum. Sci. Technol. 47, 640-665.
[19] Sirocchi, V., Caprioli, G., Ricciutelli, M., Vittori, S., Sagratini, G., 2014. Simultaneous determination of ten underivatized biogenic amines in meat by liquid chromatography-tandem mass spectrometry (HPLC-MS/MS). J. Mass Spectrom 49, 819-825.
[20] Li, R., Cai, L., Gao, T., Li, C., Zhou, G., Ye, K., 2020. Comparing the quality characteristics and bacterial communities in meatballs with or without blown pack spoilage. LWT 130,109529.
[21] Zou, W., Tang, Y., Zeng, H., Wang, C., Wu, Y., 2021. Porous Co_3O_4 nanodisks as robust peroxidase mimetics in an ultrasensitive colorimetric sensor for the rapid detection of multiple heavy metal residues in environmental water samples. J. Hazard. Mater. 417, 125994.
[22] Hu, Y., Ma, X., Zhang, Y., Che, Y., Zhao, J., 2015. Detection of amines with fluorescent nanotubes: applications in the assessment of meat spoilage. ACS Sens. 1, 22-25.
[23] Leelasreea, T., Aggarwal, H., 2022. MOF sensors for food safety: ultralow

679 detection of putrescine and cadaverine in protein rich foods. J. Mater. Chem. C 10,
680 2121-2127.
681 [24] Li, Z., Suslick, K.S., 2016. Portable optoelectronic nose for monitoring meat
682 freshness. ACS Sens. 1, 1330-1335.
683 [25] Rock, F., Barsan, N., Weimar, U., 2008. Electronic nose: current status and future
684 trends. Chem. Rev. 108, 705-725.
685 [26] Dey, A., 2018. Semiconductor metal oxide gas sensors: A review, Mater. Sci. Eng.
686 B 229, 206-217.
687 [27] Deng, J., Zhang, R., Wang, L., Lou, Z., Zhang, T., 2015. Enhanced sensing
688 performance of the Co_3O_4 hierarchical nanorods to NH_3 gas. Sens. Actuators B:
689 Chem. 209, 449-455.
690 [28] Wang, L., Lou, Z., Zhang, R., Zhou, T., Deng, J., Zhang, T., 2016. Hybrid
691 Co_3O_4/SnO_2 core-shell nanospheres as real-time rapid-response sensors for
692 ammonia gas. ACS Appl. Mater. Interfaces 8, 6539-6545.
693 [29] Schaude, C., Meindl, C., Frohlich, E., Attard, J., Mohr, G.J., 2017. Developing a
694 sensor layer for the optical detection of amines during food spoilage. Talanta 170,
695 481-487.
696 [30] Siripongpreda, T., Siralertmukul, K., Rodthongkum, N., 2020. Colorimetric sensor
697 and LDI-MS detection of biogenic amines in food spoilage based on porous PLA
698 and graphene oxide. Food Chem. 329, 127165.
699 [31] Fillol, J.L., Codolà, Z., Garcia-Bosch, I., Gómez, L., Pla, J.J., Costas, M., 2011.
700 Efficient water oxidation catalysts based on readily available iron coordination
701 complexes. Nat. Chem. 3, 807-813.
702 [32] Sy, A., Bhatti, A.I., Hamidouche, F., Le Bacq, O., Lecarme, L., Leprêtre, J.C., 2020.
703 Correlation of electrochemical and ab initio investigations of iron poly-bipyridine
704 coordination complexes for battery applications: impact of the anionic
705 environment and the local geometries of the redox complexes on the
706 electrochemical response. Phys. Chem. Chem. Phys. 22, 24077-24085.
707 [33] Bond, C.J., Sokolow, G.E., Crawley, M.R., Burns, P.J., Cox, J.M., Mayilmurugan,
708 R., Morrow, J.R., 2019. Exploring inner-sphere water interactions of Fe(II) and
709 Co(II) complexes of 12-membered macrocycles to develop CEST MRI probes.
710 Inorg. Chem. 58, 8710-8719.
711 [34] Li, X., Liu, Y., Zhang, C., Wen, T., Zhuang, L., Wang, X., Song, G., Chen, D., Ai,
712 Y., Hayat, T., Wang, X., 2018. Porous Fe_2O_3 microcubes derived from metal
713 organic frameworks for efficient elimination of organic pollutants and heavy metal
714 ions. Chem. Eng. J. 336, 241-252.
715 [35] Gütlich, P., Garcia, Y., Goodwin, H.A., 2000. Spin crossover phenomena in Fe(ii)
716 complexes, Chem. Soc. Rev. 29, 419-427.
717 [36] Develioglu, A., Resines-Urien, E., Poloni, R., Martín-Pérez, L., Costa, J.S.,
718 Burzuri, E., 2021. Tunable proton conductivity and color in a nonporous
719 coordination polymer via lattice accommodation to small molecules. Adv. Sci. 8,
720 2102619.
721 [37] Naik, A.D., Robeyns, K., Meunier, C.F., Léonard, A.F., Rotaru, A., Tinant, B.,
722 Filinchuk, Y., Su, B.L., Garcia., Y., 2014. Selective and reusable iron(II)-based

molecular sensor for the vapor-phase detection of alcohols. Inorg. Chem. 53, 1263-1265.
[38] Guo, Y., Xue, S., Dîrtu, M.M., Garcia, Y., 2018. A versatile iron(ii)-based colorimetric sensor for the vapor-phase detection of alcohols and toxic gases. J. Mater. Chem. C 6, 3895-3900.
[39] Xue, S., Wang, L., Naik, A.D., Oláh, J., Robeyns, K., Rotaru, A., Guo, Y., Garcia, Y., 2021. Iron(II) pillared-layer responsive frameworks via “kagomé dual” (kgd) supramolecular tessellations. Inorg. Chem. Front. 8, 3532-3546.
[40] Guan, Y.F., Wang, D.Y., Dong, W., 2007. Diaquabis[5-(1H-tetrazol-5-ylaminokN4)-1H-tetrazolato-kN1] iron(II) dihydrate. Acta Crystallogr. E63 (2007) m3150.
[41] Nakamoto, T., Yosihioka, M., Tanaka, Y., Kobayashi, K., Moriizumi, T., Ueyama, S., Yerazunis, W.S., 2006. Colorimetric method for odor discrimination using dye-coated plate and multiLED sensor, Sens. Actuators B: Chem. 116, 202-206.
[42] Paknahad, M., McIntosh, C., Hoorfar, M., 2019. Selective detection of volatile organic compounds in microfluidic gas detectors based on "like dissolves like", Sci. Rep. 9, 1-11.
[43] Li, Z., Wang, Z., Khan, J., LaGasse, M.K., Suslick, K.S., 2020. Ultrasensitive monitoring of museum airborne pollutants using a silver nanoparticle sensor array. ACS Sens. 5, 2783-2791.
[44] Qiao, L., Tang, X., Dong, J., 2017. A feasibility quantification study of total volatile basic nitrogen (TVB-N) content in duck meat for freshness evaluation. Food Chem. 237, 1179-1185.
[45] Coe, B.J., Harris, J.A., Brunschwig, B.S., Asselberghs, I., Clays, K., Garín, J., Orduna, J., 2005. Three-dimensional nonlinear optical chromophores based on metal-to-ligand charge-transfer from ruthenium(II) or iron(II) centers. J. Am. Chem. Soc. 127, 13399–13410.
[46] Sun, L., Rotaru, A., Robeyns, K., Garcia, Y., 2021. A colorimetric sensor for the highly selective, ultra-sensitive, and rapid detection of volatile organic compounds and hazardous gases. Ind. Eng. Chem. Res. 60, 8788-8798.
[47] Suslick, K.S., Rakow, N.A., Sen, A., 2004. Colorimetric sensor arrays for molecular recognition. Tetrahedron 60, 11133-11138.
[48] Liu, D, Liu, M., Liu, G., Zhang, S., Wu, Y., Zhang, X., 2010. Dual-channel sensing of volatile organic compounds with semiconducting nanoparticles. Anal. Chem. 82, 66-68.
[49] Li, B., Liu, J., Shi, G., Liu, J., 2013. A research on detection and identification of volatile organic compounds utilizing cataluminescence-based sensor array. Sens. Actuators B: Chem. 177, 1167-1172.
[50] Ward Jr, J. H., 1963. Hierarchical grouping to optimize an objective function. J. Am. Stat. Assoc. 58, 236-244.
[51] Ashley, K., O’Connor P.F., Eds., 2017. The national institute for occupational safety and health (NIOSH)-manual of analytical methods (NMAM™), 5th ed. Cincinnati, U. S. A. 2017.
[52] Chen, P. L., Liu, I.P., Chen, W. C., Niu, J. S., Liu, W. C., 2020. Study of a platinum

nanoparticle (PtNP)/amorphous In-Ga-Zn-O (A-IGZO) thin-film-based ammonia gas sensor. Sens. Actuators B Chem. 332, 128592.
[53] Das, R., Pradhan, S., Biswas, S., Sharma, P., Ghosh, A., Bandyopadhyay, R., Pramanik, P., 2014. Aliphatic amines vapours detection by quartz crystal microbalance sensor. Sens. Actuators B Chem. 198, 94–101.
[54] Chen, E.X., Fu, H.R., Lin, R., Tan, Y.X., Zhang, J., 2014. Highly selective and sensitive trimethylamine gas sensor based on cobalt imidazolate framework material. ACS Appl. Mater. Interfaces 6, 22871-22875.
[55] Diaz, Y.J., Page, Z.A., Knight, A.S., Treat, N.J., Hemme, J.R., Hawker, C.J., Alaniz, J.R.d., 2017. A versatile and highly selective colorimetric sensor for the detection of amines, Chem. Eur. J. 23, 3562 –3566.
[56] Sarkar, T., Ashraf, P.M., Srinives, S., Mulchandani, A., 2018. Calixarene-functionalized single-walled carbon nanotubes for sensitive detection of volatile amines. Sens. Actuators B Chem. 268, 115-122.
[57] Zhang, H., Luo, Y., Zhuo, M., Yang, T., Liang, J., Zhang, M., Ma, J., Duan, H., Li, Q., 2016. Diethylamine gas sensor using V_2O_5-decorated α-Fe_2O_3 nanorods as a sensing material. RSC Adv. 6, 6511-6515.
[58] Bueno, L., Meloni, G.N., Reddy, S.M., Paixao, T.R.L.C., 2015. Use of plastic-based analytical device, smartphone and chemometric tools to discriminate amines. RSC Adv. 5, 20148-20154.
[59] Jin, Y.J., Kwak, G., 2018. Detection of biogenic amines using a nitrated conjugated polymer. Sens. Actuators B Chem. 271, 183-188.
[60] Huang, Y., Liu, X., Wang, Q., Fu, J., Zhao, L., Liu, Z., Jin, D., 2017. Highly responsive ethylenediamine vapor sensor based on a perylenediimide–camphorsulfonic acid complex via ionic self-assembly. J. Mater. Chem. C 5, 7644-7651.
[61] Dong, Z.P., Zhao, J.J., Liu, P.Y., Liu, Z.L., Wang, Y.Q., 2019. A metal–organic framework constructed by a viologen-derived ligand: photochromism and discernible detection of volatile amine vapors. New J. Chem. 43, 9032-9038.
[62] Ghollasi-Mood, F., Mohsenzadeh, M., Housaindokht, M.R., Varidi, M., 2017. Microbial and chemical spoilage of chicken meat during storage at isothermal and fluctuation temperature under aerobic conditions. Iran. J. Appl. Anim. Sci. 8, 38-46.
[63] Musto, C.J., Lim, S.H., Suslick, K.S., 2009. Colorimetric detection and identification of natural and artificial sweeteners. Anal. Chem., 81, 6526–6533.
[64] Carey, J.R., Suslick, K.S., Hulkower, K.I., Imlay,J.A., Imlay, KR., Ingison, C.K., Ponder, J.B., Sen, A., Wittrig, A.E., 2011. Rapid identification of bacteria with a disposable colorimetric sensing array. J. Am. Chem. Soc. 133, 7571-7576.
[65] Magnaghi, L.R., Capone, F., Zanoni, C., Alberti, G., Quadrelli, P., Biesuz, R., 2020. Colorimetric sensor array for monitoring, modelling and comparing spoilage processes of different meat and fish foods. Foods 9, 684.
[66] Thi, A.N.T., Sampers, I., Haute, S.V., Samapundo, S., Nguyen, B.L., Heyndrickx, M., Devlieghere, F., 2015. Decontamination of Pangasius fish (Pangasius hypophthalmus) with chlorine or peracetic acid in the laboratory and in a

Vietnamese processing company. Int. J. Food Microbiol. 208, 93-101.
[67] Zhang, G., Loch, A.S., Kistemaker, J.C.M., Burn, P.L., Shaw, P.E., 2020. Dicyanovinyl-based fluorescent sensors for dual mechanism amine sensing, J. Mater. Chem. C 8, 13723-13732.
[68] Hu, Y., Zhou, Z., Zhao, F., Liu, X., Gong, Y., Xiong, W., Sillanpää, M., 2018. Fingerprint detection and differentiation of gas-phase amines using a fluorescent sensor array assembled from asymmetric perylene diimides. Sci. Rep. 8,10277.
[69] Chayavanich, K., Thiraphibundet, P., A. Imyim, A., 2020. Biocompatible film sensors containing red radish extract for meat spoilage observation. Spectrochim. Acta A Mol. Biomol. Spectrosc. 226, 117601.